

1 Connection between encounter volume and diffusivity in geophysical flows

2 Irina I. Rypina¹, Stefan G. Llewellyn Smith², and Larry J. Pratt¹

3 ¹Physical Oceanography Department, Woods Hole Oceanographic Institution, 266 Woods Hole
4 Rd., Woods Hole, MA 02543

5 ²Department of Mechanical and Aerospace Engineering, Jacobs School of Engineering and
6 Scripps Institution of Oceanography, UCSD, 9500 Gilman Dr., La Jolla, CA 92093-0411

7 Corresponding author's email: irypina@whoi.edu

8 **Abstract:** Trajectory encounter volume – the volume of fluid that passes close to a reference
9 fluid parcel over some time interval – has been recently introduced as a measure of mixing
10 potential of a flow. Diffusivity is the most commonly used characteristic of turbulent diffusion.
11 We derive the analytical relationship between the encounter volume and diffusivity under the
12 assumption of an isotropic random walk, i.e. diffusive motion, in one and two dimensions. We
13 apply the derived formulas to produce maps of encounter volume and the corresponding
14 diffusivity in the Gulf Stream region of the North Atlantic based on satellite altimetry, and
15 discuss the mixing properties of Gulf Stream rings. Advantages offered by the derived formula
16 for estimating diffusivity from oceanographic data are discussed, as well as applications to other
17 disciplines.

18 1. Introduction

19 The frequency of close encounters between different objects or organisms can be a fundamental
20 metric in social and mechanical systems. The chances that a person will meet a new friend or
21 contract a new disease during the course of a day is influenced by the number of distinct
22 individuals that he or she comes into close contact with. The chances that a predator will ingest a
23 poisonous prey, or that a mushroom hunter will mistakenly pick up a poisonous variety, is
24 influenced by the number of distinct species or variety of prey or mushrooms that are
25 encountered. In fluid systems, the exchange of properties such as temperature, salinity or
26 humidity between a given fluid element and its surroundings is influenced by the number of
27 other distinct fluid elements that pass close by over a given time period. In all these cases it is
28 best to think of close encounters as providing the *potential*, if not necessarily the act, of
29 transmission of germs, toxins, heat, salinity, etc...

30 In cases of property exchange within continuous media such as air or water, it may be most
31 meaningful to talk about a mass or volume passing within some radius of a reference fluid
32 element as this element moves along its trajectory. Rypina and Pratt (2017) introduce a trajectory
33 encounter volume, V , the volume of fluid that comes in contact with the reference fluid parcel
34 over a finite time interval. The increase of V over time is one measure of the mixing potential of
35 the element, “mixing” being the irreversible exchange of properties between different water

36 parcels. Thus, fluid parcels that have large encounter volumes as they move through the flow
 37 field have large mixing potential, i.e., an opportunity to exchange properties with other fluid
 38 parcels, and vice versa.

39 In order to formally define the encounter volume V , Rypina and Pratt (2017) subdivide the entire
 40 fluid into infinitesimal fluid elements with volumes dV_i , and define the encounter volume for
 41 each fluid element to be the total volume of fluid that passes within a radius R of it over a finite
 42 time interval $t_0 < t < t_0 + T$, i.e.,

$$43 \quad V(\vec{x}_0; t_0, T, R) = \lim_{dV_i \rightarrow 0} \sum_i dV_i. \quad (1)$$

44 In practice, for dense uniform grids of trajectories, $\vec{x}_k(\vec{x}_{0k}; t_0, T)$, $k = 1, \dots, K$, where t_0 is the
 45 starting time, T is the trajectory integration time, and \vec{x}_{0k} is the trajectory initial position
 46 satisfying $\vec{x}(\vec{x}_0, t_0; T = 0) = \vec{x}_0$, both the limit and the subscript in the above definition (1) can
 47 be dropped. In this case, the encounter volume can be approximated by

$$48 \quad V \approx N \delta V, \quad (2)$$

49 where the *encounter number*,

$$50 \quad N(\vec{x}_{0ref}; t_0, T, R) = \sum_{k \neq ref}^K I(\min(|\vec{x}_k(\vec{x}_{0k}; t_0, T) - \vec{x}_{ref}(\vec{x}_{0ref}; t_0, T)|) \leq R), \quad (3)$$

51 is the number of trajectories that come within a radius R of the reference trajectory,
 52 $\vec{x}_{ref}(\vec{x}_{0ref}; t_0, T)$, over a time $t_0 < t < t_0 + T$. Here the indicator function I is 1 if true and 0 if
 53 false, and K is the total number of particles. As in Rypina and Pratt (2017), we define encounter
 54 volume based on the number of encounters with different trajectories, not the total number of
 55 encounter events (see the schematic diagram of trajectory encounters in Fig. 1). Rypina and Pratt
 56 (2017) discuss how the encounter volume can be used to identify Lagrangian Coherent
 57 Structures (LCS) such as stable and unstable manifolds of hyperbolic trajectories and regions
 58 foliated by the KAM-like tori surrounding elliptic trajectories in realistic geophysical flows. A
 59 detailed comparison between the encounter volume method and some other Lagrangian methods
 60 of LCS identification, as well as the dependences on parameters, t_0 , T , R , and on grid spacing (or
 61 on the number of trajectories, K), and the relative advantages of different techniques, was given
 62 in Rypina and Pratt (2017). The interested reader is referred to that earlier paper for details. The
 63 current paper is concerned only with the question of finding the connection between the
 64 encounter volume and diffusivity, rather than identifying LCS.

65 Given the seemingly fundamental importance of close encounters, it is of interest to relate
 66 metrics such as V to other bulk measures of interactions within the system. For example, in some
 67 cases it may be more feasible to count encounters rather than to measure interactions or property
 68 exchanges directly, whereas in other cases the number of encounters might be most pertinent to

69 the process in question but difficult to measure directly. In many applications, including ocean
70 turbulence, the most commonly used metric of mixing is the eddy diffusivity, κ , a quantity that
71 relates transport of fluid elements by turbulent eddies to diffusion (LaCasce, 2008; Vallis, 2006;
72 Rypina et al., 2015; Kamenkovich et al., 2015). The underlying assumption is that the eddy field
73 drives downgradient tracer transfer, similar to molecular diffusion but with a different (larger)
74 diffusion coefficient. This diffusive parameterization of eddies has been implemented in many
75 non-eddy-resolving oceanic numerical models. The diffusivity can be measured by a variety of
76 means, including dye release (Ledwell et al., 2000; Sundermeyer and Ledwell, 2001; Rypina et
77 al., 2016), surface drifter dispersion (Okubo, 1971; Davis, 1991; LaCasce, 2008, La Casce et al.,
78 2014; Rypina et al. 2012; 2016), and property budgets (Munk, 1966). In numerical models κ is
79 often assumed constant in both time and space, or related in some simplified manner to the large-
80 scale flow properties (Visbeck, 1997).

81 Because the purpose of the diffusivity coefficient κ is to quantify the intensity of the eddy-
82 induced tracer transfer, i.e., the intensity of mixing, it is tempting to relate it to the encounter
83 volume, V , which quantifies the mixing potential of a flow and thus is closely related to tracer
84 mixing. Such an analytical connection between the encounter volume and diffusivity could
85 potentially also be useful for the parameterizations of eddy effects in numerical models. The
86 main goal of this paper is to develop a relationship between V and κ in one and two dimensions.
87 Specifically, we seek an analytical expression for the encounter volume, V , i.e., the volume of
88 fluid that passed within radius R from a reference particle over time, as a function of κ . The
89 relationship is not as straightforward as one might first imagine, but can nevertheless be written
90 down straightforwardly in the long-time limit. This is opportune, since the concept of eddy
91 diffusivity is most relevant in the long-time limit.

92 2. Connection between encounter volume and diffusivity

93 This problem was framed in mathematical terms in Rypina and Pratt (2017), who outlined some
94 initial steps towards deriving the analytical connection between encounter volume and diffusivity
95 but did not finish the derivation. In this section, we complete the derivation.

96 2.1. Main idea for the derivation

97 Let us start by considering the simplest diffusive random walk process in one or two dimensions,
98 where particles take steps of fixed length Δx in random directions along the x-axis in 1D or
99 along both x- and y-axes in 2D, respectively, at fixed time intervals Δt .

100 The single particle dispersion, i.e., the ensemble-averaged square displacement from the
101 particle's initial position, is $D_{1D} = \langle (x - x_0)^2 \rangle$ and $D_{2D} = \langle (x - x_0)^2 + (y - y_0)^2 \rangle$ in 1D
102 or 2D, respectively. For a diffusive process, the dispersion grows linearly with time, and the
103 constant proportionality coefficient related to diffusivity. Specifically, $D_{1D} = 2\kappa_{1D}t$ with
104 $\kappa_{1D} = \Delta x^2 / (2\Delta t)$, and $D_{2D} = 4\kappa_{2D}t$ with $\kappa_{2D} = \Delta x^2 / (4\Delta t)$.

105 It is convenient to consider the motion in a reference frame that is moving with the reference
 106 particle. In that reference frame, the reference particle will always stay at the origin, while other
 107 particles will still be involved in a random walk motion, but with a diffusivity twice that in the
 108 stationary frame, $\kappa^{moving}=2\kappa^{stationary}$ (Rypina and Pratt, 2017).

109 The problem of finding the encounter number then reduces to counting the number of randomly
 110 walking particles (with diffusivity κ^{moving}) that come within radius R of the origin in the
 111 moving frame. This is related to a classic problem in statistics – the problem of a random walker
 112 reaching an absorbing boundary, usually referred to as “a cliff” (because once a walker reaches
 113 the absorbing boundary, it falls off the cliff), over a time interval from 0 to t .

114 In the next section we will provide formal solutions; here we simply outline the steps to
 115 streamline the derivation. We start by deriving the appropriate diffusion equation for the
 116 probability density function, $p(\vec{x}, t)$, of random walkers in 1D or 2D:

$$117 \quad \frac{\partial p}{\partial t} = \kappa \nabla^2 p. \quad (4)$$

118 We place a cliff, \vec{x}_c , at the perimeter of the encounter sphere, i.e., at a distance R from the
 119 origin, and impose an absorbing boundary condition at a cliff,

$$120 \quad p(\vec{x}_c, t) = 0, \quad (5a)$$

121 which removes (or “absorbs”) particles that have reached the cliff (see Fig. 2 for a schematic
 122 diagram). We then consider a random walker that is initially located at a point \vec{x}_0 outside the
 123 cliff at $t = 0$, i.e.,

$$124 \quad p(\vec{x}, t = 0) = \delta(\vec{x} - \vec{x}_0), \quad (5b)$$

125 and we write an analytical solution for the probability density function satisfying Eqs. (4-5),

$$126 \quad G(\vec{x}, t; \vec{x}_0, \vec{x}_c), \quad (6)$$

127 that quantifies the probability to find a random walker initially located at \vec{x}_0 at any location \vec{x}
 128 outside of the cliff at a later time $t > 0$. In mathematical terms, G is the Green’s function of the
 129 diffusion equation.

130 The survival probability, which quantifies the probability that a random walker initially located
 131 at \vec{x}_0 at $t = 0$ has “survived” over time t without falling off the cliff, is

$$132 \quad S(t; \vec{x}_0, \vec{x}_c) = \int G(\vec{x}, t; \vec{x}_0, \vec{x}_c) d\vec{x}, \quad (7)$$

133 where the integral is taken over all locations outside of the cliff. The encounter, or “non-
 134 survival”, probability can then be written as the conjugate quantity,

135 $P_{en}(t; \vec{x}_0, \vec{x}_c) = 1 - S(t; \vec{x}_0, \vec{x}_c),$ (8)

136 which quantifies the probability that a random walker initially located at \vec{x}_0 at $t = 0$ has
 137 reached, or fallen off, the cliff over time t . This allows one to write the encounter volume, i.e.,
 138 the volume occupied by particles that were initially located outside of the cliff and that have
 139 reached the cliff by time t , as

140 $V(t; \vec{x}_c) = \int P_{en}(t; \vec{x}_0, \vec{x}_c) d\vec{x}_0,$ (9)

141 where the integral is taken over all initial positions outside of the cliff.

142
 143 2.2. 1D case

144 Consider a random walker initially located at the origin, who takes, with a probability $\frac{1}{2}$, a fixed
 145 step Δx to the right or to the left along the x -axis after each time interval Δt . Then the probability
 146 to find a walker at a location $x = n\Delta x$ at after $(m + 1)$ steps is

147 $p(n\Delta x, (m + 1)\Delta t) = 1/2[p((n - 1)\Delta x, m\Delta t) + p((n + 1)\Delta x, m\Delta t)].$ (10)

148 Using a Taylor series expansion in Δx and Δt , we can write down the finite-difference
 149 approximation to the above expression as

$$p(x, t) + \Delta t \frac{\partial p}{\partial t} = \frac{1}{2} \left[p(x, t) - \Delta x \frac{\partial p}{\partial x} + \frac{\Delta x^2}{2} \frac{\partial^2 p}{\partial x^2} + p(x, t) + \Delta x \frac{\partial p}{\partial x} + \frac{\Delta x^2}{2} \frac{\partial^2 p}{\partial x^2} + O(\Delta x^4) \right] =$$

150 $= p(x, t) + \frac{\Delta x^2}{2} \frac{\partial^2 p}{\partial x^2} + O(\Delta x^4),$ (11)

151 yielding a diffusion equation

152 $\frac{\partial p}{\partial t} = \kappa \frac{\partial^2 p}{\partial x^2}$ (12)

153 with diffusivity coefficient $\kappa = \frac{\Delta x^2}{2\Delta t}$.

154

155 A Green's function for the 1D diffusion equation without a cliff is a solution with initial
 156 condition $p(x, t = 0; x_0) = \delta(x - x_0)$ in an unbounded domain. It takes the form

157 $G_{unbounded}(x, t; x_0) = \frac{1}{\sqrt{4\pi\kappa t}} e^{-\frac{(x-x_0)^2}{4\kappa t}}.$ (13)

158 A Green's function with the cliff (see Fig. 2 for a schematic diagram), for a solution to the
 159 initial-value problem with $p(x, t = 0; x_0) = \delta(x - x_0)$ in a semi-infinite domain, $x \in [-\infty; x_c]$,

160 with an absorbing boundary condition at a cliff, $p(x = x_c, t; x_0) = 0$, can be constructed by the
 161 method of images from two unbounded Green's functions as

$$162 \quad G(x, t; x_0, x_c) = \frac{1}{\sqrt{4\pi\kappa t}} \left(e^{-\frac{(x-x_0)^2}{4\kappa t}} - e^{-\frac{(x-(2x_c-x_0))^2}{4\kappa t}} \right). \quad (14)$$

163 It follows from (7-9) that the survival or non-encounter probability is

$$164 \quad S(t; x_0, x_c) := \int_{-\infty}^{x_c} G(x, t; x_0, x_c) dx = \text{Erf} \left[\frac{x_c - x_0}{2\sqrt{\kappa t}} \right], \quad (15)$$

165 the encounter probability is

$$166 \quad P_{en}(t; x_0, x_c) = 1 - S(t) = 1 - \text{Erf} \left(\frac{x_c - x_0}{2\sqrt{\kappa t}} \right), \quad (16)$$

167 and the encounter volume is

$$168 \quad V(t; x_c) = \int_{-\infty}^{x_c} P_{en}(t; x_0, x_c) dx_0 = \int_{-\infty}^{x_c} \left(1 - \text{Erf} \left[\frac{x_c - x_0}{2\sqrt{\kappa t}} \right] \right) dx_0 = \frac{2}{\sqrt{\pi}} \sqrt{\kappa t}. \quad (17)$$

169 The above formula accounts for the randomly walking particles that have reached the cliff from
 170 the left over time t . By symmetry, if the cliff was located to the right of the origin, the same
 171 number of particles would be reaching the cliff from the right, so the total encounter volume is

$$172 \quad V(t; x_c) = \frac{4}{\sqrt{\pi}} \sqrt{\kappa t}. \quad (18)$$

173 Note that formula (18) gives the encounter volume, i.e., the volume of fluid coming within radius
 174 R from the origin, in a reference frame moving with the reference particle, so the corresponding
 175 diffusivity in the right-hand side of (18) is $\kappa^{moving} = 2\kappa^{stationary}$.

176 2.3. 2D case

177 Consider a random walker in 2D, who is initially located at the origin and who takes, with a
 178 probability of 1/4, a fixed step of length Δx to the right, left, up or down after each time interval
 179 Δt . Then the probability to find a walker at a location $x = n\Delta x, y = m\Delta y$ at time $t = (l + 1)\Delta t$
 180 is

$$181 \quad p(n\Delta x, m\Delta y, (l + 1)\Delta t) = \frac{1}{4} \left[p((n - 1)\Delta x, m\Delta y, l\Delta t) + p((n + 1)\Delta x, m\Delta y, l\Delta t) + \right. \\
 182 \quad \left. p(n\Delta x, (m - 1)\Delta y, l\Delta t) + p(n\Delta x, (m + 1)\Delta y, l\Delta t) \right]. \quad (19)$$

183 Using a Taylor series expansion in $\Delta x, \Delta y$ and Δt , the finite-difference approximation leads to a
 184 diffusion equation

$$185 \quad \frac{\partial p}{\partial t} = \kappa \left(\frac{\partial^2 p}{\partial x^2} + \frac{\partial^2 p}{\partial y^2} \right) \quad (20)$$

186 with diffusivity coefficient $\kappa = \frac{\Delta x^2}{4\Delta t}$.

187 To proceed, we need an analytical expression for the Green's function of Eq. (20) with a cliff at a
 188 distance R from the origin, i.e., a solution to the initial-value problem with $p(\vec{x}, t = 0; \vec{x}_0) =$
 189 $\delta(\vec{x} - \vec{x}_0)$ for the above 2D diffusion equation on a semi-infinite plane ($r \geq R, 0 < \theta \leq 2\pi$),
 190 bounded internally by an absorbing boundary (a cliff) located at $r = R$, so that $p(r =$
 191 $R, \theta, t; \vec{x}_0) = 0$ (see Fig. 2(right) for a schematic diagram). Here (r, θ) are polar coordinates.

192 Carslaw and Joeger (1939) give the answer as

$$193 \quad G(r, \theta, t; r_0, \theta_0, R) = u + w = \sum_{n=-\infty}^{\infty} (u_n(r, t; r_0, R) + w_n(r, t; r_0, R)) \cos n(\theta - \theta_0) \quad (21)$$

194 where $r_0 (\geq R), \theta_0$ denote the source location, and

$$195 \quad \{u_n, w_n\} = L^{-1} \{\bar{u}_n, \bar{w}_n\} = \frac{1}{2\pi i} \lim_{T \rightarrow \infty} \int_{\gamma-iT}^{\gamma+iT} e^{st} \{\bar{u}_n, \bar{w}_n\} ds$$

196 are the inverse Laplace transforms of

$$197 \quad \bar{u}_n = \frac{1}{2\pi\kappa} \begin{cases} I_n(qr)K_n(qr_0), R < r < r_0 \\ I_n(qr_0)K_n(qr), r > r_0 \end{cases} \text{ and } \bar{w}_n = -\frac{I_n(qR)}{K_n(qR)} K_n(qr_0)K_n(qr) \quad (22)$$

$$198 \quad \text{with } q = \sqrt{\frac{s}{\kappa}}.$$

199 The survival probability (from Eq. (7)) is

$$200 \quad S(t; r_0, R) = \int_{R^2} G(\vec{x}, t; \vec{x}_0, R) d^2\vec{x} = \int_0^{2\pi} \int_R^\infty \sum_{n=-\infty}^{\infty} (u_n + v_n) \cos n(\theta - \theta_0) r dr d\theta =$$

$$201 \quad 2\pi \int_R^\infty (u_0 + v_0) r dr. \quad (23)$$

202 Next, we take the Laplace transform of the survival probability and write it in terms of a Laplace
 203 variable s as

$$204 \quad \bar{S}(s, r_0, R) = \int_0^\infty e^{-st} S(t; r_0, R) dt = 2\pi \int_R^\infty (\bar{u}_0 + \bar{w}_0) r dr = \frac{1}{\kappa} \int_R^{r_0} I_0(qr)K_0(qr_0) r dr +$$

$$205 \quad \frac{1}{\kappa} \int_{r_0}^\infty I_0(qr_0)K_0(qr) r dr - \frac{1}{\kappa} \int_R^\infty \frac{I_0(qR)}{K_0(qR)} K_0(qr)K_0(qr_0) r dr. \quad (24)$$

206 Using $\int r I_0(r) dr = r I_1(r)$ and $\int r K_0(r) dr = -r K_1(r)$, and $\lim_{x \rightarrow \infty} x K_1(x) = 0$ we find

$$207 \quad \bar{S}(s; r_0, R) =$$

$$208 \quad \frac{1}{\kappa} K_0(qr_0) \left[\frac{r}{q} I_1(qr) \right] \Big|_R^{r_0} + \frac{1}{\kappa} I_0(qr_0) \left[-\frac{r}{q} K_1(qr) \right] \Big|_R^\infty - \frac{1}{\kappa} \frac{I_0(qR)}{K_0(qR)} K_0(qr_0) \left[-\frac{r}{q} K_1(qr) \right] \Big|_R^\infty =$$

$$209 \quad \frac{1}{\kappa} \left\{ \frac{r_0}{q} (I_1(qr_0)K_0(qr_0) + I_0(qr_0)K_1(qr_0)) - \frac{a}{q} \frac{K_0(qr_0)}{K_0(qR)} (I_1(qR)K_0(qR) + I_0(qR)K_1(qR)) \right\}. \quad (25)$$

211 But $I_1(x)K_0(x) + I_0(x)K_1(x) = \frac{1}{x}$ so

$$212 \quad \bar{S}(s; r_0, R) = \frac{1}{\kappa} \left(\frac{1}{q^2} - \frac{1}{q^2} \frac{K_0(qr_0)}{K_0(qR)} \right) = \frac{1}{s} \left(1 - \frac{K_0(qr_0)}{K_0(qR)} \right). \quad (26)$$

213 From (8), the encounter probability $P_{en}(t; \vec{x}_0, R) = 1 - S(t; \vec{x}_0, R)$, and from (9) the encounter
214 volume is

$$215 \quad V(t; R) = \int_{R^2} P_{en} d^2 \vec{x}_0 = \int_0^{2\pi} \int_R^\infty P_{en} r_0 dr_0 = 2\pi \int_R^\infty [1 - S(t; r_0, R)] r_0 dr_0. \quad (27)$$

216 We now take the Laplace transform of the encounter number to get

$$217 \quad \bar{V}(s; R) = \int_0^\infty e^{-st} V(t; R) dt = 2\pi \int_R^\infty \left[\frac{1}{s} - \bar{S}(s; R) \right] r_0 dr_0 = 2\pi \int_R^\infty \frac{K_0(qr_0)}{K_0(qR)} \frac{r_0}{s} dr_0 =$$

$$218 \quad \frac{2\pi}{sK_0(qR)} \left[-\frac{r_0}{q} K_1(qr_0) \right] \Big|_R^\infty = \frac{2\pi R K_1(qR)}{sq K_0(qR)} = \frac{2\pi R}{s^{3/2} \kappa^{-\frac{1}{2}} K_0\left(\sqrt{\frac{s}{\kappa}} R\right)}, \quad (28)$$

219 where we used $\int_0^\infty e^{-st} dt = \frac{1}{s}$, $\int K_0(z)z dz = -zK_1(z)$, and $\lim_{z \rightarrow \infty} K_1(z) = 0$.

220 The explicit connection between the encounter volume and diffusivity is thus given by the
221 inverse Laplace transform of the above expression (28),

$$222 \quad V(t; R) = L^{-1}\{\bar{V}(s; R)\}. \quad (29)$$

223 Although numerically straightforward to evaluate, a non-integral analytic form does not exist for
224 this inverse Laplace transform. To better understand the connection between V and κ and the
225 growth of V with time, we next look at the asymptotic limits of small and large time. The small- t
226 limit is transparent, while the long- t limit is more involved.

227 (a) small- t asymptotics

228 In the small- t limit, the corresponding Laplace coordinate s is large, giving

$$229 \quad \bar{V}(s; R) \sim 2\pi R \kappa^{\frac{1}{2}} \frac{1}{s^{3/2}} \quad (30)$$

230 because $\lim_{z \rightarrow \infty} \frac{K_1(z)}{K_0(z)} = 1$. Noting that $L^{-1}\left\{s^{-\frac{3}{2}}\right\} = \frac{2\sqrt{t}}{\sqrt{\pi}}$, the inverse Laplace transform of the
231 above gives the following simple expression connecting the encounter number and diffusivity at
232 short times:

$$233 \quad V(t; R) \xrightarrow{t \rightarrow 0} 4R\sqrt{\pi} \sqrt{\kappa t}. \quad (31)$$

234 (b) large- t asymptotics

235 In the large- t limit, the Laplace coordinate s is small and the asymptotic expansions K_0, K_1 take
 236 the form

$$237 \quad \lim_{z \rightarrow 0} K_0(z) = -\gamma - \ln\left(\frac{z}{2}\right) + O\left(\left(\frac{z}{2}\right)^2 \ln\left(\frac{z}{2}\right)\right), \quad (32)$$

$$238 \quad \lim_{z \rightarrow 0} K_1(z) = \frac{1}{z} + \frac{z}{2} \left[\ln\left(\frac{z}{2}\right) + \gamma - \frac{1}{2} \right] + O(z^3 \ln z), \quad (33)$$

239 giving

$$240 \quad \lim_{s \rightarrow 0} \bar{V}(s; R) = -\frac{4\pi\kappa}{s^2 \ln(\tau s)} - \frac{\pi R^2}{s} + O\left(\frac{1}{s \ln(\tau s)}\right), \quad (34)$$

241 where

$$242 \quad \tau = \frac{R^2 e^{2\gamma}}{4\kappa}. \quad (35)$$

243 We now need to take an inverse Laplace transform of \bar{V} . The second term in the right-hand side
 244 gives $L^{-1}\left\{\frac{\pi R^2}{s}\right\} = \pi R^2$. Llewelyn Smith (2000) discusses the literature for inverse Laplace
 245 transforms of the form $(s^\alpha \ln s)^{-1}$ for small s . For our problem, the discussion in Olver (1974,
 246 Chap. 8, §11.4) is the most helpful approach. His result (11.13), discarding the exponential term
 247 which is not needed here, shows that the inverse Laplace transform of $(s^2 \ln s)^{-1}$ has the
 248 asymptotic expansion

$$249 \quad L^{-1}\left\{\frac{1}{s^2 \ln s}\right\} \xrightarrow{t \rightarrow \infty} -t \left(\frac{1}{\ln t} + \frac{1-\gamma}{(\ln t)^2} + O((\ln t)^{-3}) \right). \quad (36)$$

250 Using $L^{-1}\{F(\tau s)\} = \frac{1}{\tau} f(t/\tau)$, we thus obtain the desired connection between the encounter
 251 number and diffusivity at long times:

$$252 \quad V(t; R) \xrightarrow{t \rightarrow \infty} 4\pi\kappa t \left(\frac{1}{\ln \frac{t}{\tau}} + \frac{1-\gamma}{(\ln \frac{t}{\tau})^2} \right) - \pi R^2 + O\left(\frac{t}{(\ln \frac{t}{\tau})^3}\right) + O\left(\frac{1}{\ln \frac{t}{\tau}}\right). \quad (37)$$

253 Physically, the time scale τ (Eq. (35)) defines the time at which the dispersion of random
 254 particles, $D = 4\kappa\tau$, is comparable to the volume of the encounter sphere, ie., $R^2 e^{2\gamma} \cong \pi R^2$ in
 255 2D. Thus for $t \gg \tau$, particles are coming to the encounter sphere “from far away.”

256 For practical applications, it is sufficient to only keep the leading order term of the expansion,
 257 yielding a simpler connection between encounter number and diffusivity,

$$258 \quad V(t; R) \xrightarrow{t \rightarrow \infty} \frac{4\pi\kappa t}{\ln \frac{t}{\tau}} + O\left(\frac{t}{(\ln \frac{t}{\tau})^2}\right). \quad (38)$$

259 Note again that the diffusivity in the right-hand side of Eqs. (28-29), (31) and (38) is
260 $\kappa^{moving}=2\kappa^{stationary}$.

261 2.4. Numerical tests of the derived formulas in 1d and 2d

262 Before applying our results to the realistic oceanic flow, we numerically tested the accuracy of
263 the derived formulas in idealized settings by numerically simulating a random walk motion in 1D
264 and 2D, as described in the beginning of subsections 2.1 and 2.2, respectively. We then
265 computed the encounter number and encounter volume using definition (2-3), and compared the
266 result with the derived exact formulas (18) and (28-29) and with the asymptotic formulas (31)
267 and (38). Note that although formulas (28-29) are exact, the inverse Laplace transform still needs
268 to be evaluated numerically and thus is subject to numerical accuracy, round-off errors etc.; these
269 numerical errors are, however, small, and we will refer to numerical solutions of (28-29) as
270 “exact,” as opposed to the asymptotic solutions (31) and (38).

271 The comparison between numerical simulations and theory is shown in Fig. 3. Because the
272 numerically simulated random walk deviates significantly from the diffusive regime over short
273 ($< O(100\Delta t)$) time scales, the agreement between numerical simulation and theory is poor at
274 those times in both 1D and 2D. Once the random walkers have executed > 100 time steps,
275 however, the dispersion reaches the diffusive regime, and the agreement between the theory (red)
276 and numerical simulation (black) rapidly improves for both 1D and 2D cases, with the two
277 curves approaching each other at long times. In 2D, the long-time asymptotic formula (38) works
278 well at long times, $t \gg \tau$, as expected. The 2D short-time asymptotic formula (green) agrees well
279 with the exact formula (red) at short times but not with the numerical simulations (black) for the
280 same reason as discussed above, i.e., because the numerically simulated random walk has not yet
281 reached the diffusive regime at those times.

282 3. Application to the altimetric velocities in the Gulf Stream region

283 Sea surface height measurements made from altimetric satellites provide nearly global estimates
284 of geostrophic currents throughout the World Oceans. These velocity fields, previously
285 distributed by AVISO, are now available from the Copernicus Marine and Environment
286 Monitoring Service (CMEMS) website (<http://marine.copernicus.eu/>), both along satellite tracks
287 and as a gridded mapped product in both near-real and delayed time. Here we use the delayed-
288 time gridded maps of absolute geostrophic velocities with $\frac{1}{4}$ deg spatial resolution and temporal
289 step of 1 day, and focus our attention on the Gulf Stream extension region of the North Atlantic
290 Ocean. There, the Gulf Stream separates from the coast and starts to meander, shedding cold-
291 and warm-core Gulf Stream rings from its southern and northern flanks. These rings are among
292 the strongest mesoscale eddies in the ocean. However, their coherence, interaction with each
293 other and with other flow features, and their contribution to transport, stirring and mixing are still
294 not completely understood (Bower et al., 1985; Cherian and Brink, 2016).

295 Maps showing the encounter volume for fluid parcel trajectories in the region, and the
296 corresponding diffusivity estimates (Fig. 4) could be useful both for understanding and
297 interpreting the transport properties of the flow, as well as for benchmarking and
298 parameterization of eddy effects in numerical models. In our numerical simulations, trajectories
299 were released on a regular grid with $dx = dy \cong 10$ km on 11 Jan 2015 and were integrated
300 forward in time for 90 days using a fifth-order variable-step Runge-Kutta integration scheme
301 with bi-linear interpolation between grid points in space and time. The encounter radius was
302 chosen to be $R = 30$ km in both zonal and meridional directions, i.e., about a third of a radius of
303 a typical Gulf Stream ring. Similar parameter values were used in Rypina and Pratt (2017),
304 although our new simulation was carried out using more recent 2015 velocities instead of 1997
305 as in that paper.

306 The encounter volume field, shown in the top left panel of Fig. 4, highlights the overall
307 complexity of the flow and identifies a variety of features with different mixing potential, most
308 notably several Gulf Stream rings with spatially small low- V (blue) cores and larger high- V (red)
309 peripheries. Although the azimuthal velocities and vorticity-to-strain ratio are large within the
310 rings, the coherent core regions with inhibited mixing potential are small, suggesting that the
311 *coherent* transport by these rings might be smaller than anticipated from the Eulerian diagnostics
312 such as the Okubo-Weiss or closed-streamline criteria (Chelton et al., 2011; Abernathey and
313 Haller, 2017). On the other hand, the rings' peripheries, where the mixing potential is elevated
314 compared to the surrounding fluid, cover a larger geographical area than the cores. Thus, while
315 rings inhibit mixing within their small cores, the enhanced mixing on the periphery might be
316 their dominant effect. This is consistent with the results from Rypina and Pratt (2017), but a
317 more thorough analysis is needed to test this hypothesis. Notably, the encounter number is also
318 large along the northern and southern flank of the Gulf Stream jet, with two separate red curves
319 running parallel to each other and a valley in between (although the curves could not be traced
320 continuously throughout the entire region). This enhanced mixing on both flanks of the Gulf
321 Stream Extension current is reminiscent of chaotic advection driven by the tangled stable and
322 unstable manifolds at the sides of the jet (del-Castillo-Negrete and Morrison, 1993; Rogerson et
323 al., 1999; Rypina et al., 2007; Rypina and Pratt, 2017), and is also consistent with the existence
324 of critical layers (Kuo, 1949; Ngan and Sheppard, 1997).

325
326 We now apply the asymptotic formula (38) to convert the encounter volume to diffusivity.
327 Because equation (38) is not invertible analytically, we converted V to κ numerically using a
328 look-up table approach. More specifically, we used (38) to compute theoretically-predicted V
329 values at time $T=90$ days for a wide range of κ 's spanning all possible oceanographic values for
330 0 to 10^9 cm^2/s , and we used the resulting look-up table to assign the corresponding κ values to
331 V values in the 3rd row of Fig. 4. Note that, instead of the long-time asymptotic formula (38) (as
332 in in the 3rd row of Fig. 4), it is also possible to use the exact formulas (28-29) to convert V to κ
333 via a table look-up approach. The resulting exact diffusivities, shown in the 2nd row of Fig. 4, are
334 similar to the long-time asymptotic values (3rd row). Because both exact and asymptotic formulas

335 were derived under the assumption of a diffusive random walk, neither should work well in
336 regions with a non-diffusive behavior. The asymptotic formula has the advantage of being
337 simpler and it also provides for a numerical estimate of the “long-time-limit” time scale, τ ,
338 shown in the bottom row of Fig. 4

339
340 As expected, the diffusivity maps in the 2nd and 3rd rows of Fig. 4, which resulted from
341 converting V to κ using (28-29) or (38), respectively, have the same spatial variability as the V -
342 map, with large κ at the peripheries of the Gulf Stream rings and at the flanks of the Gulf Stream
343 and small κ at the cores of the rings, near the Gulf Stream centerline and far away from the Gulf
344 Stream current, where the flow is generally slower. The diffusivity values range from
345 $O(10^5) \text{ cm}^2/\text{s}$ to $O(10^7) \text{ cm}^2/\text{s}$. Using the 1971 Okubo’s diffusivity diagram and scaling law,
346 $\kappa_{Okubo}[\text{cm}^2/\text{s}] = 0.0103 l[\text{cm}]^{1.15}$, our diffusivity values correspond to spatial scales from
347 10 km to 650 km , thus spanning the entire mesoscale range. This is not surprising considering
348 the Lagrangian nature of our analysis, where trajectories inside the small ($< 50 \text{ km}$) low-
349 diffusion eddy cores stay within the cores for the entire integration duration (90 days), whereas
350 trajectories in the high-diffusivity regions near the ring peripheries and at the flanks of the Gulf
351 Stream jet cover large distances, sometimes $> 650 \text{ km}$, over 90 days.

352
353 The performances of the exact and asymptotic diffusive formulas vary greatly throughout the
354 domain, with better/poorer performances in high-/low- V areas. This is because in the low- V
355 areas, the behavior of fluid parcels is non-diffusive, so the diffusive theoretical formulas work
356 poorly. The breakdown of the long-time asymptotic formula is evident in the 4th row of Fig. 4,
357 which shows the corresponding long-time scales, τ (from Eq. (35)), throughout the domain. As
358 suggested by our 2D random walk simulations, the long-time asymptotic diffusive formula only
359 works well when $t \gg \tau$, but in reality τ values are < 9 days (1/10 of our integration time) only in
360 the highest- V regions, and are much larger everywhere else, reaching values of $\cong 90$ days within
361 the cores of the Gulf Stream rings. More detailed comparison between theory, both exact and
362 asymptotic, and numerical $V(t)$ is shown in Fig. 5 for 3 reference trajectories that are initially
363 located inside the core, on the periphery, and outside of a Gulf Stream ring (black, red, and blue,
364 respectively) centered at approximately 36.8N and 60W. Clearly, the diffusive theory works
365 poorly for the trajectory inside the eddy core (black curve). The agreement is better for the blue
366 and even better for the red curves, corresponding to trajectories outside and on the periphery of
367 the eddy, although deviations between the theory and numerics are still visible, raising questions
368 about the general validity of the diffusive approximation in ocean flows on time scales of a few
369 months.

370
371 The non-diffusive nature of the parcel motion over 90 days is because ocean eddies have finite
372 length- and time-scales, so a variety of different transport regimes generally occurs before
373 separating parcels become uncorrelated and transport becomes diffusive, as in a random walk. At
374 very short times the motion of fluid parcels is largely governed by the local velocity shear, so the

375 resulting transport regime is ballistic, i.e., $D \propto T^2$ and $V \propto T$ (Rypina and Pratt, 2017). At longer
376 times, when velocity shear can no longer be assumed constant in space and time, the regime may
377 transition to a local Richardson regime (i.e., $D \propto t^3$), where separation at a given scale is
378 governed by the local features of a comparable scale (Richardson 1926; Bennett 1984; Beron-
379 Vera and LaCasce 2016), or to a non-local chaotic-advection spreading regime (i.e., $D \propto$
380 $\exp(\lambda t)$), where separation is governed by the large scale flow features (Bennett 1984; Rypina et
381 al. 2010; Beron-Vera and LaCasce 2016). The kinetic energy spectrum of a flow indicates
382 whether a local or non-local regime will be relevant. The chaotic transport regime is generally
383 expected to occur in mesoscale-dominated eddying flows, such as, for example, AVISO velocity
384 fields, over time scales of a few eddy winding times. At times long enough for particles to
385 sample many different flow features, such as Gulf Stream meanders or mesoscale eddies in the
386 AVISO fields, the velocities of the neighboring particles become completely uncorrelated, and
387 transport finally approaches the diffusive regime. With the mesoscale eddy turnover time being
388 on the order of several weeks, it often takes longer than 90 days to reach the diffusive regime.

389
390 A number of diffusivity estimates other than Okubo's have been made for the Gulf Stream
391 extension region (e.g., Zhurbas and Oh, 2004; LaCasce, 2008; Rypina et al., 2012; Abernathey
392 and Marshall, 2013; Klocker and Abernathey, 2014; or Cole et al., 2015). These estimates are
393 based on surface drifters (Zhurbas and Oh, 2004, LaCasce, 2008; Rypina et al., 2012), satellite-
394 observed velocity fields (Abernathey and Marshall, 2013; Klocker and Abernathey, 2014,
395 Rypina et al., 2012), and Argo float observations (Cole et al., 2015), and they use either the
396 spread of drifters or the evolution of simulated or observed tracer fields to deduce diffusivity.
397 The resulting diffusivities are spatially varying and span 2 orders of magnitude, from 2×10^4
398 m^2/s in the most energetic regions in the immediate vicinity of the Gulf Stream and its
399 extension, to $10^3 m^2/s$ in less energetic areas, to $200 m^2/s$ in the coastal areas of the Slope Sea.
400 Diffusivity estimates vary significantly depending on the initial tracer distribution used
401 (Abernathey and Marshall, 2013) and depend on whether the suppression by the mean current
402 has been taken into account (Klocker and Abernathey, 2014). The diffusivity tensor has also
403 been shown to be anisotropic, with a large anisotropy ratio near the Gulf Stream (Rypina et al.,
404 2012). Data resolution and coverage, as well as the choice of time and length scales also play a
405 role in defining κ value (Cole et al., 2015). All of these issues complicate the reconciliation of
406 different diffusivity estimates. Nevertheless, ignoring these complications for a moment, and
407 avoiding the smallest diffusivities in those geographical areas of Fig. 4 where the diffusive
408 approximation is invalid, our $O(10^3 m^2/s)$ encounter-volume-based diffusivity estimates tend to
409 be in the middle of the range of available estimates for the western North Atlantic. Although not
410 inconsistent with other estimates, the encounter volume method did not predict diffusivities to
411 reach values of $10^4 m^2/s$ anywhere within the considered geographical domain.

412
413 Because the action of the real ocean velocity field on drifters or tracers is generally not exactly
414 diffusive, all methods simply fit the diffusive approximation to the corresponding variable of

415 interest, such as particle dispersion, tracer variance, or, in our case, encounter volume. The
 416 analytic form of the diffusive approximation is, however, different for different variables and
 417 different flow regimes. For example, for a diffusive random walk regime, dispersion grows
 418 linearly with time, whereas the growth of the encounter volume is non-linear, as defined by eq.
 419 (38). This generally leads to different diffusivity estimates resulting from different methods. In
 420 other words, the diffusivity value that fits best to the observed particle dispersion at 90 days does
 421 not necessarily provide the best fit to the observed encounter volume at 90 days, and vice versa.

422

423 To illustrate this more rigorously, we consider a linear strain flow,

$$u = \alpha x,$$

$$v = -\alpha y,$$

424

425 with a constant strain coefficient α . The particle trajectories are given by $x = x_0 e^{\alpha t}$, $y = y_0 e^{-\alpha t}$
 426 where x_0, y_0 are particles initial positions. The dispersion of a small cluster of particles that are
 427 initially uniformly distributed within a small square of side length $2dx$ is

428

$$D = \langle (X - \bar{X})^2 + (Y - \bar{Y})^2 \rangle,$$

429

429 where $X = x - x_0$ and $Y = y - y_0$ are displacements of particles from their initial positions and
 430 the overbar denotes the ensemble mean. Since the linear strain velocity remains unchanged in a
 431 reference frame moving with a particle, without loss of generality we can restrict our attention to
 432 a cluster that is initially centered at the origin, so $\bar{X} = \bar{Y} = 0$. In the long time limit, when
 433 $e^{\alpha t} \gg 1 \gg e^{-\alpha t}$, the dispersion becomes

434

$$D = 2/3 dx^3 e^{2\alpha t}.$$

435 If one is using a diffusive fit,

436

$$D = 4\kappa_D t,$$

437 to approximate diffusivity, then the resulting diffusivity is

$$\kappa_D = \frac{dx^3 e^{2\alpha t}}{6t}.$$

438

On the other hand, the encounter volume for the linear strain flow is

439

$$V = 2\alpha R^2 t,$$

440

whereas the long-time diffusive fit is

441

$$V = \frac{4\pi\kappa_V t}{\ln t/\tau},$$

442

yielding

$$\kappa_V = -\frac{\alpha R^2 \text{ProductLog}\left(-\frac{\pi e^{2\gamma}}{2\alpha t}\right)}{2\pi}$$

443

444 where the function $\text{ProductLog}(z)$ is a solution to $z = we^w$. Because κ_D is exponential in time,
 445 while κ_V is not, κ_D always becomes larger than κ_V at large t .

446

447 Of course, real oceanic flows are more complex than the simple linear strain example. However,
 448 for flows that are in a state of chaotic advection, exponential separation between neighboring

449 particles will occur and the dispersion will grow exponentially in time, as in the linear strain
 450 example. Although we do not have a formula for the encounter volume for a chaotic advection
 451 regime, the linear strain example suggests that the encounter volume growth will likely be slower
 452 than exponential. Thus, for a chaotic advection regime, the dispersion-based diffusivity could be
 453 expected to be larger than the encounter-volume-based diffusivity. This can potentially explain
 454 the smaller encounter-volume-based diffusivity values in Fig. 4 compared to other available
 455 estimates from the literature. Numerical simulations (not shown) using an analytic Duffing
 456 oscillator flow, which features chaotic advection, indeed produced smaller encounter-volume-
 457 based diffusivity than dispersion-based diffusivity, in agreement with our arguments above. The
 458 AVISO velocities are dominated by the meso- rather than submeso-scales, and the 90-day time
 459 interval is about a few mesoscale eddy winding times, thus this flow satisfies all the pre-
 460 requisites for the chaotic advection to occur. Finally, the particle trajectories that we used to
 461 produce Fig. 4 can be grouped into small clusters (we are using encounter radius $R=30$ km as a
 462 cluster radius for consistency) to estimate their dispersion and infer diffusivity from its slope.
 463 Consistent with our arguments above, the resulting dispersion-based diffusivities in Fig. 6 are
 464 larger than the encounter-volume-based diffusivities in Fig. 4 and reach values $O(10^4 \text{ m}^2/\text{s})$ in
 465 the energetic regions of the Gulf Stream and its extension, in agreement with the previous
 466 diffusivity estimates from the literature. In applications where the number of encounters is a
 467 more important quantity than the spread of particles, the encounter-volume-based diffusivity
 468 might be a more appropriate estimate to use.

469
 470 In the left panels of Fig. 4 we used the full velocity field to advect trajectories, so both the mean
 471 and the eddies contributed to the resulting encounter volumes and the corresponding
 472 diffusivities. But what is the contribution of the eddy field alone to this process? To answer this
 473 question, we have performed an additional simulation in the spirit of Rypina et al. (2012), where
 474 we advected trajectories using the altimetric time-mean velocity field, and then subtracted the
 475 resulting encounter volume, V_{mean} , from the full encounter number, V . The result characterizes
 476 the contribution of eddies, although strictly speaking $V_{eddy} \neq V - V_{mean}$ because of non-
 477 linearity. Note also that because we are interested in the Lagrangian-averaged effects of eddies
 478 following fluid parcels, V_{eddy} cannot be estimated by simply advecting particles by the local
 479 eddy field alone (see an extended discussion of this effect in Rypina et al., 2012). Not
 480 surprisingly, the eddy-induced encounter volumes (upper right panel of Fig. 4) are smaller than
 481 the full encounter numbers, with the largest decrease near the Gulf Stream current, where both
 482 the mean velocity and the mean shear are large. In other geographical areas, specifically at the
 483 peripheries of the Gulf Stream rings, the decrease in V is less significant, so the resulting map
 484 retains its overall qualitative spatial structure. The same is true for the diffusivities in the 2nd and
 485 3rd rows of Fig. 4. The overall spatial structure of the eddy diffusivity is preserved and matches
 486 that in left panels, but the values decrease, with the largest differences near the Gulf Stream,
 487 where some diffusivity values are now $O(10^6) \text{ cm}^2/\text{s}$ instead of $O(10^7) \text{ cm}^2/\text{s}$. In contrast, κ
 488 only decreases, on average, by a factor of 2 (instead of an order of magnitude) near the

489 peripheries of the Gulf Stream rings. The long-time diffusive time scale τ generally increases,
490 and the ratio t/τ generally decreases throughout the domain, but the long-time asymptotic
491 formula (38) still works well in high- V regions, specifically on the peripheries of the Gulf Stream
492 rings where τ is still significantly less than t .

493 494 4. Discussion and Summary

495 With many new diagnostics being developed for characterizing mixing in fluid flows, it is
496 important to connect them to the well-established conventional techniques. This paper is
497 concerned with understanding the connection between the encounter volume, which quantifies
498 the mixing potential of the flow, and diffusivity, which quantifies the intensity of the down-
499 gradient transfer of properties. Intuitively, both quantities characterize mixing and it is natural to
500 expect a relationship between them, at least in some limiting sense. Here, we derived this
501 anticipated connection for a diffusive process, and we showed how this connection can be used
502 to produce maps of spatially-varying diffusivity, and to gain new insights into the mixing
503 properties of eddies and the particle spreading regime in realistic oceanic flows.

504 When applied to the altimetry-based velocities in the Gulf Stream region, the encounter volume
505 and diffusivity maps show a number of interesting physical phenomena related to transport and
506 mixing. Of particular interest are the transport properties of the Gulf Stream rings. The
507 materially-coherent Lagrangian cores of these rings, characterized by very small diffusivity, are
508 smaller than expected from earlier Eulerian diagnostics (Chelton et al., 2011). The periphery
509 regions with enhanced diffusivity are, on the other hand, large, raising a question about whether
510 the rings, on average, act to preserve coherent blobs of water properties or to speed up the
511 mixing. The encounter volume, through the derived connection to diffusivity, might provide a
512 way to address this question and to quantify the two effects, clarifying the role of eddies in
513 transport and mixing.

514 Our encounter-volume-based diffusivity estimates are within the range of other available
515 estimates from the literature, but are not among the highest. We provided an intuitive explanation
516 for why the encounter-volume-based diffusivities might be smaller than the dispersion-based
517 diffusivities, and we supported our explanation with theoretical developments based on a linear
518 strain flow, and with numerical simulations. We note that in problems where the encounters
519 between particles are of interest, rather than the particle spreading, the encounter-volume-based
520 diffusivities would be more appropriate to use than the conventional dispersion-based estimates.

521 Reliable data-based estimates of eddy diffusivity are needed for parameterizations in numerical
522 models. The conventional estimation of diffusivity from Lagrangian trajectories via calculating
523 particle dispersion requires large numbers of drifters or floats (LaCasce, 2008). It would be
524 useful to have a technique that would work with fewer instruments. The derived connection
525 between encounter volume and diffusivity might help in achieving this goal. Specifically, one
526 could imagine that if an individual drifting buoy was equipped with an instrument that would

527 measure its encounter volume – the volume of fluid that came in contact with the buoy over time
528 t – then the resulting encounter volume could be converted to diffusivity using the derived
529 connection. This would allow estimating diffusivity using a single instrument.

530 In the field of social encounters, it is becoming possible to construct large data sets by tracking
531 cell phones, smart transit cards (Sun, et al. 2013), and bank notes (Brockmann, et al. 2006). As
532 was the case for the Gulf Stream trajectories, some of the behavior appears to be diffusive and
533 some not so. Where diffusive/random walk behavior is relevant, it may be easier to accumulate
534 data on close encounters rather than on other metrics using, for example, autonomous vehicles
535 and instruments that are able, through local detection capability, to count foreign objects that
536 come within a certain range.

537 **Acknowledgments:** This work was supported by the NSF grants OCE-1558806 and EAR-
538 1520825, and NASA grant NNX14AH29G.

539

540

541

542

543

544

545

546

547

548

549

550

551

552

553

554

555 **References**

- 556 Abernathey, R. P., and G. Haller (2018). Transport by Lagrangian Vortices in the
557 Eastern Pacific. *J. Phys. Oceanogr.* doi:10.1175/JPO-D-17-0102.1, in press.
- 558
- 559 Abernathey, R. P., and J. Marshall (2013). Global surface eddy diffusivities derived from
560 satellite altimetry, *J. Geophys. Res. Oceans*, 118, 901-916, doi:10.1002/jgrc.20066.
- 561
- 562 Bennett, A. F. (1984). Relative dispersion: Local and nonlocal dynamics. *J. Atmos. Sci.*, 41,
563 1881-1886, doi:10.1175/1520-0469(1984)041<1881:RDLAND.2.0.CO;2.
- 564
- 565 Beron-Vera, F. J., and J. H. LaCasce (2016). Statistics of simulated and observed pair separation
566 in the Gulf of Mexico. *J. Phys. Oceanogr.*, 46, 2183-2199, [https://doi.org/10.1175/JPO-D-15-](https://doi.org/10.1175/JPO-D-15-0127.1)
567 0127.1
- 568
- 569 Bower., A. S., H. T. Rossby, and J. L. Lillibridge (1985). The Gulf Stream-Barrier or blender? *J.*
570 *Phys. Oceanogr.*, 15, 24-32.
- 571
- 572 Brockmann, D., L. Hufnagel, T. Geisel (2006). The scaling laws of human travel. *Nature*
573 439(7075):462-465.
- 574
- 575 Carslaw, H. S.; Jaeger, J. C. (1939). On Green's functions in the theory of heat conduction. *Bull.*
576 *Amer. Math. Soc.* 45 (1939), no. 6, 407-413.<https://projecteuclid.org/euclid.bams/1183501899>
- 577
- 578 Cherian, D.A. and K.H. Brink (2016). Offshore Transport of Shelf Water by Deep-Ocean Eddies.
579 *J. Phys. Oceanogr.*, 46, 3599-3621, <https://doi.org/10.1175/JPO-D-16-0085.1>
- 580
- 581 Chelton, D. B., M. G. Schlax, and R. M Samelson (2011). Global observations of nonlinear
582 mesoscale eddies. *Prog. Oceanogr.*, 91, 167-216
- 583
- 584 Cole, S. T., C. Wortham, E. Kunze, and W. B. Owens (2015). Eddy stirring and horizontal
585 diffusivity from Argo float observations: Geographic and depth variability, *Geophys. Res. Lett.*,
586 42, 3989-3997, doi:10.1002/2015GL063827.
- 587
- 588 del-Castillo-Negrete, D. and P. J. Morrison (1993). Chaotic transport of Rossby waves in shear
589 flow. *Phys. Fluids A*, 5 (4), 948-965.
- 590
- 591 Davis, R. E. (1991). Observing the general circulation with floats. *Deep-Sea Res.*, 38, 531-571.
- 592 d'Ovidio F., Fernandez V., Hernandez-Garcia E., Lopez C. (2004). Mixing structures in the
593 Mediterranean Sea from finite size Lyapunov exponents. *Geophys. Res. Lett.* 31:L17203
- 594
- 595 Froyland, G., Padberg, K., England, M. H., and Treguier, A. M. (2007). Detection of coherent
596 oceanic structures via transfer operators, *Phys. Rev. Lett.*, 98, 224503,
597 doi:10.1103/PhysRevLett.98.224503
- 598
- 599 Haller, G., Hadjighasem, A., Farazmand, M., and Huhn, F. (2016). Defining coherent vortices
600 objectively from the vorticity, *J. Fluid Mech.*, 795, 136–173, doi:10.1017/jfm.2016.151, 2016.

601
602 Kamenkovich, I., I. I. Rypina, and P. Berloff (2015). Properties and Origins of the Anisotropic
603 Eddy-Induced Transport in the North Atlantic. *Journal of Physical Oceanography*, 45, 778-791,
604 doi:10.1175/JPO-D-14-0164.1.

605
606 Klocker, A., and R. Abernathey, (2014). Global Patterns of Mesoscale Eddy Properties and
607 Diffusivities. *JPO*, 44, 1030-1046, doi: 10.1175/JPO-D-13-0159.1

608 Kuo, H., (1949). Dynamic instability of two-dimensional non-divergent flow in a barotropic
609 atmosphere. *J. Meteor.*, 6, 105-122

610
611 LaCasce, J. H. (2008). Statistics from Lagrangian observations. *Prog. Oceanogr.*, 77, 1-29,
612 doi:10.1016/j.pocean.2008.02.002.

613
614 LaCasce, J. H., Ferrari, r., Marshall, J., Tulloch,R., Balwada, D. & Speer, K. (2014). Float-
615 derived isopycnal diffusivities in the DIMES experiment. *Journal of Physical*
616 *Oceanography*. ISSN 0022-3670. 44(2), s 764-780. doi: 10.1175/JPO-D-13-0175.1

617
618 Ledwell, J. R., A. J. Watson, and C. S. Law (1998). Mixing of a tracer in the pycnocline, *J.*
619 *Geophys. Res.*, 103(C10), 21499-21529, doi:10.1029/98JC01738.

620
621 Ledwell, J. R., E. T. Montgomery, K. L. Polzin, L. C. St. Laurent, R. W. Schmitt & J. M. Toole,
622 (2000). Evidence for enhanced mixing over rough topography in the abyssal ocean. *Nature*, 403,
623 179-182, doi:10.1038/35003164

624
625 Llewellyn Smith, S. G. (2000). The asymptotic behaviour of Ramanujan's integral and its
626 application to two-dimensional diffusion-like equations, *Euro. Jnl of Applied Mathe-*
627 *matics*, 11, 13-28

628
629 Mendoza, C., Mancho, A. M., and Wiggins, S. (2014). Lagrangian descriptors and the
630 assessment of the predictive capacity of oceanic data sets, *Nonlin. Processes Geophys.*, 21, 677-
631 689, doi:10.5194/npg-21-677-2014

632
633 Munk, W. H. (1966). Abyssal Recipes, *Deep-Sea Res.*, 13, 707-730.

634
635 Ngan, K., and T. G. Shepherd, 1997: Chaotic mixing and transport in Rossby wave critical
636 layers. *J. Fluid Mech.*, 334, 315-351.

637
638 Okubo, A. 1971. Ocean diffusion diagram. *Deep-Sea Res.*, 18, 789-802.

639
640 Olver, F. W. J. (1974). *Asymptotics and Special Functions*. Academic.

641
642 Rogerson, A. M., P. D. Miller, L. J. Pratt, and C.K.R.T. Jones (1999). Lagrangian Motion and
643 Fluid Exchange in a Barotropic Meandering Jet. *J. Phys. Oceanogr.* 29, 2635-2655.

644

641 Richardson, L. F. (1926). Atmospheric diffusion on a distanceneighbour graph. Proc. Roy. Soc.
642 London, A110, 709-737, doi:10.1098/rspa.1926.0043.

643

644 Rypina, I. I., M. G. Brown, F. J. Beron-Vera, H. Kocak, M. J. Olascoaga, and I. A.
645 Udovydchenkov (2007). On the Lagrangian dynamics of atmospheric zonal jets and the
646 permeability of the stratospheric polar vortex. *J. Atmos. Sci.*, 64, 3595-3610.

647

648 Rypina, I. I., L. J. Pratt, J. Pullen, J. Levin, and A. Gordon (2010). Chaotic advection in an
649 archipelago. *J. Phys. Oceanogr.*, 40, 1988-2006, doi:10.1175/2010JPO4336.1.

650

651 Rypina, I. I., A. Kirincich, S. Lentz, M. Sundermeyer (2016). Investigating the eddy diffusivity
652 concept in the coastal ocean. *J. Phys. Oceanogr.*, 46(7), 2201-2218, DOI:
653 <http://dx.doi.org/10.1175/JPO-D-16-0020.1>

654

655 Rypina, I. I., and L. J. Pratt (2017). Trajectory encounter volume as a diagnostic of mixing
656 potential in fluid flows. *Nonlin. Processes Geophys.*, 24, 189-202, [https://doi.org/10.5194/npg-](https://doi.org/10.5194/npg-24-189-2017)
657 [24-189-2017](https://doi.org/10.5194/npg-24-189-2017)

658

659 Rypina, I. R., I. Kamenkovich, P. Berloff and L. J. Pratt (2012). Eddy-Induced Particle
660 Dispersion in the Near-Surface North Atlantic. *J. Phys. Ocean.* 42(12), 2206-2228, DOI:
661 10.1175/JPO-D-11-0191.1

662

663 Rypina, I. I., Scott, S. E., Pratt, L. J., and Brown, M. G. (2011). Investigating the connection
664 between complexity of isolated trajectories and Lagrangian coherent structures, *Nonlin.*
665 *Processes Geophys.*, 18, 977-987, doi:10.5194/npg-18-977-2011

666

667 Shadden, S. C., Lekien, F., and Marsden, J. E.(2005). Definition and properties of Lagrangian
668 coherent structures from finite-time Lyapunov exponents in two-dimensional aperiodic flows,
669 *Physica D*, 212, 271-304

670

671 Sun, L. K. W. Axhausen, L. Der-Horng and X Huang (2013). Understanding metropolitan
672 patterns of daily encounters. *PNAS* 110(34), 13774-13779.

673

674 Sundermeyer, M., and J. Ledwell (2001). Lateral dispersion over the continental shelf: Analysis
675 of dye release experiments. *J. Geophys. Res.*, 106, 9603–9621, doi:10.1029/2000JC900138.

676

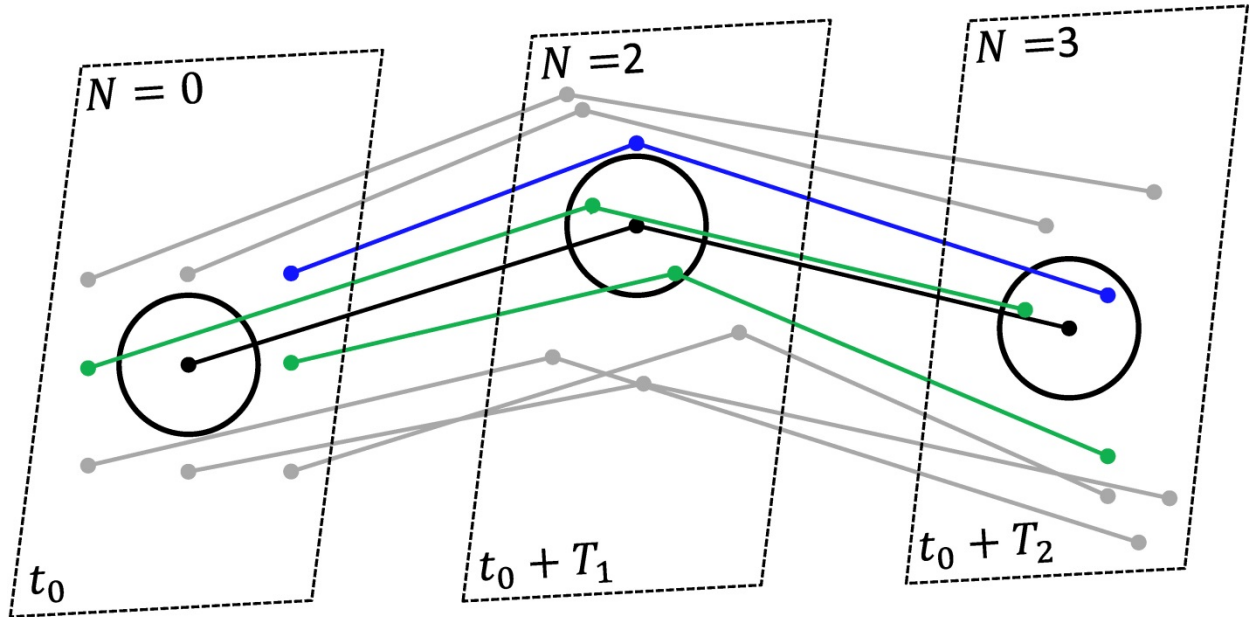
677 Vallis, G. K. (2006). *Atmospheric and Oceanic Fluid Dynamics*. Cambridge University Press,
678 745 pp.

679

680 Visbeck, M., J. Marshall, T. Haine, and M. Spall (1997). Specification of eddy transfer
681 coefficients in coarse-resolution ocean circulation models. *J. Phys. Oceanogr.*, 27, 381-402.

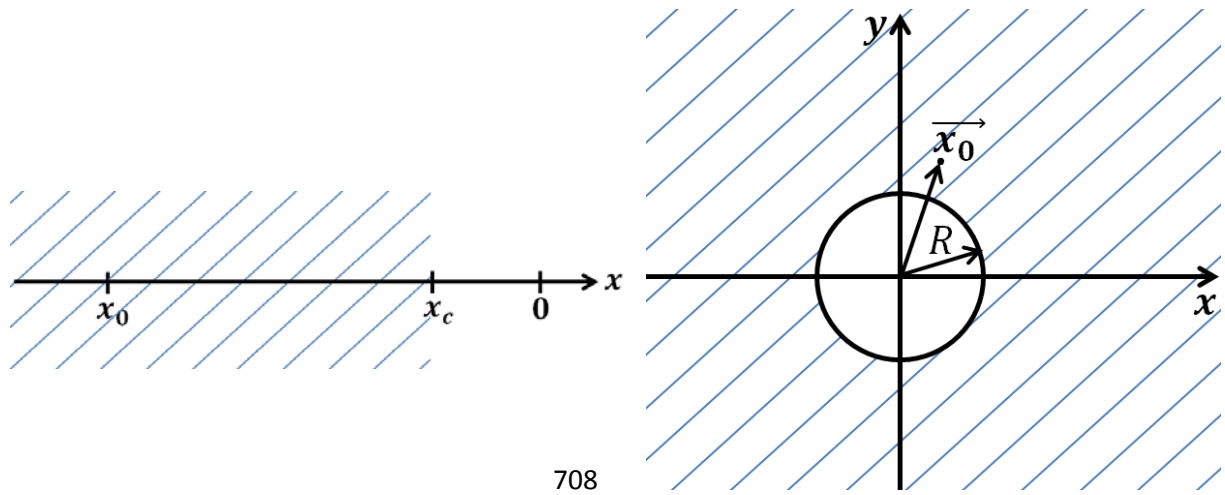
682

683 Zhurbas, V., and I. Oh (2004). Drifter-derived maps of lateral diffusivity in the Pacific and
684 Atlantic Oceans in relation to surface circulation patterns. *J. Geophys. Res.*, 109, C05015,
685 doi:10.1029/2003JC002241.



686
 687 Fig. 1. Schematic diagram of trajectory encounters, showing trajectories of 9 particles, with dots indicating
 688 positions of particles at 3 time instances, at the release time, t_0 , and at two later times, $t_0 + T_1$ and $t_0 + T_2$.
 689 The reference trajectory and the encounter sphere are shown in black, trajectories that do not encounter the
 690 reference trajectory are in grey, and trajectories that encounter the reference trajectory are in green if the
 691 encounter occur at $t_0 + T_1$, and in blue if encounters occur at $t_0 + T_2$. Time slices are schematically shown by
 692 dashed rectangles, and the encounter number, N , is indicated at the top of each time slice.
 693

694
 695
 696
 697
 698
 699
 700
 701
 702
 703
 704
 705
 706
 707



709 **Figure 2. Schematic diagram in 1D (left) and 2D (right). Hatched areas show semi-infinite domains outside of the cliff.**

710

711

712

713

714

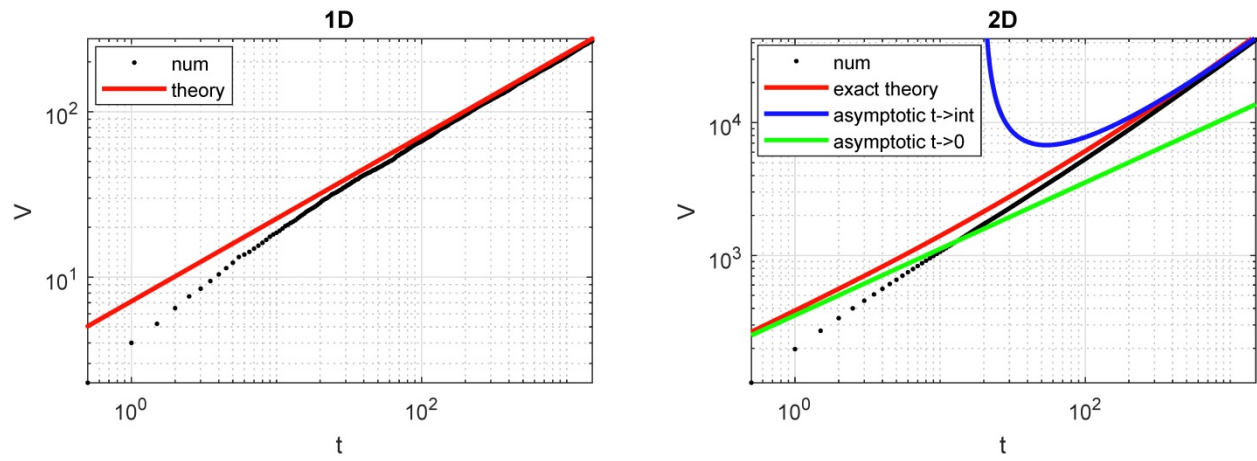
715

716

717

718

719



720

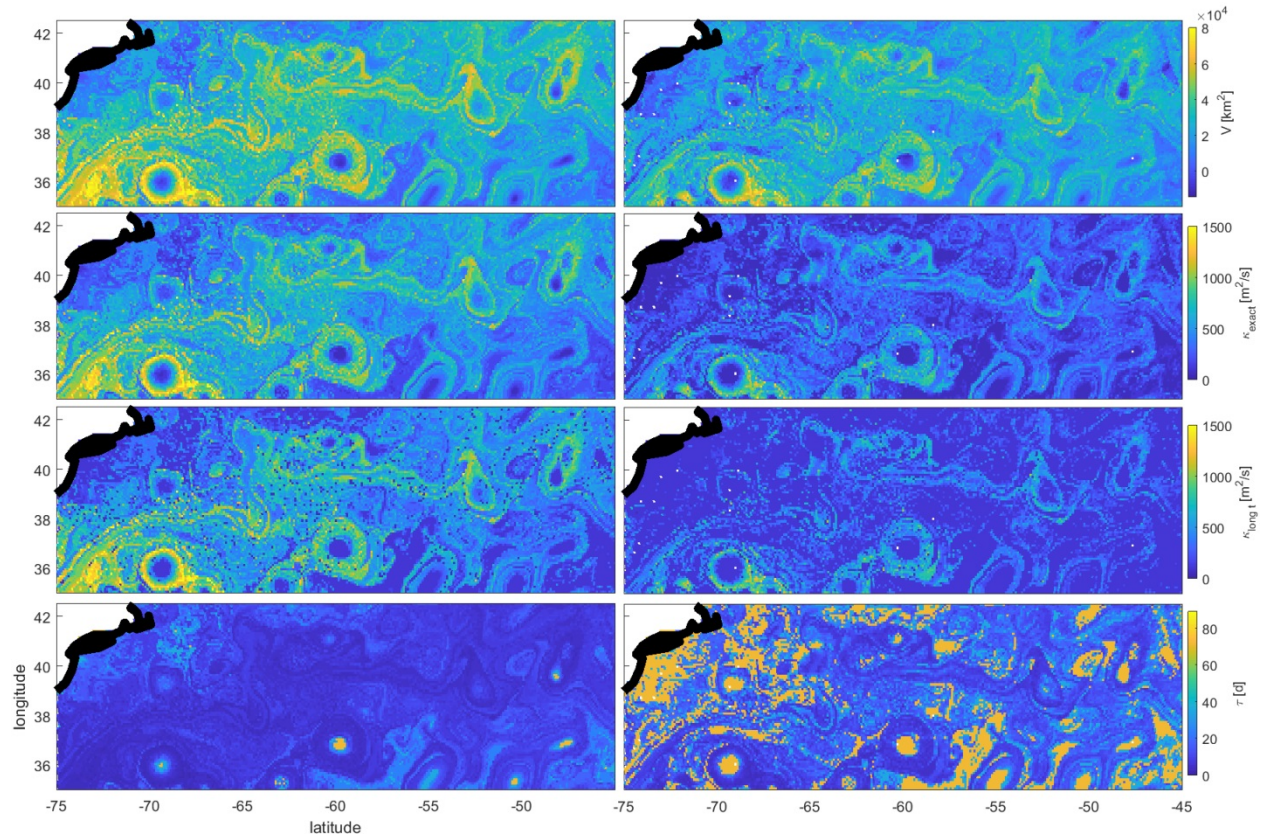
721 **Figure 3. Comparison between theoretical expression (red, green, blue) and numerical estimates (black) of the encounter**
 722 **volume for a random walk in 1D (left) and 2D (right). In both, $\kappa = 5$ and $\Delta t = 0.5$. In 2D, $\tau \cong 20$.**

723

724

725

726



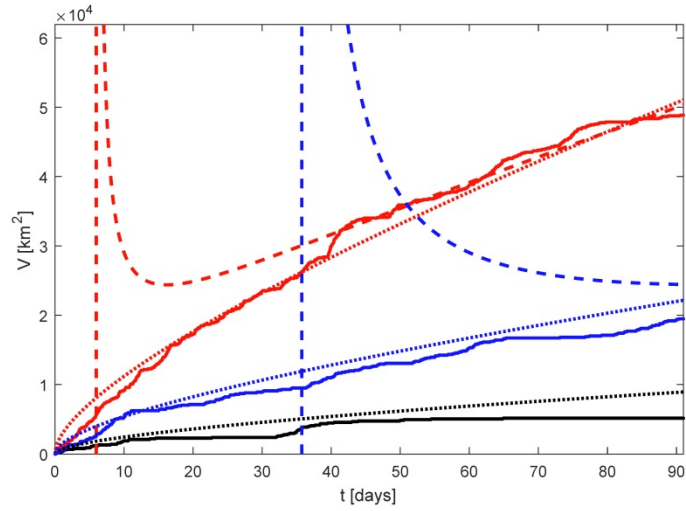
727

728 **Figure 4.** Encounter number (1st row), exact diffusivity (2nd row), long-time diffusivity (3rd row) and diffusive time-scale (4-
 729 th row) for the full flow (left) and for the eddy component of the flow (right). White shows land and thick black curve
 730 shows coastline. The encounter volume was computed on 11/01/2015 over 90 days with encounter radius of 30 km.

731

732

733



734

735 **Figure 5. Comparison between numerically-computed V (solid) and the exact (dotted) and long-time diffusive formulas**
 736 **(dashed) with the corresponding κ for the 3 reference trajectories located in the core, periphery and outside (black, red,**
 737 **blue) of a Gulf Stream ring.**

738

739

740

741

742

743

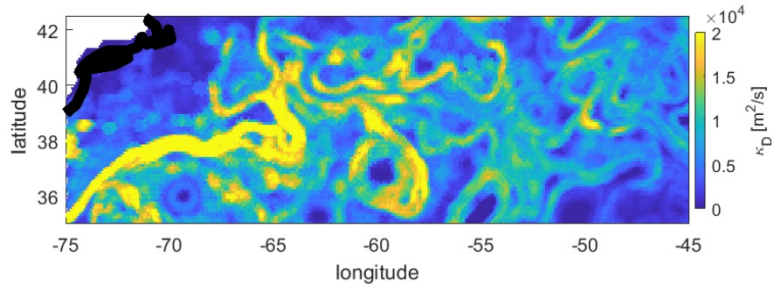
744

745

746

747

748



749

750

Figure 6. Dispersion-based diffusivity, κ_D .